

Electrophoretic Deposition of MnO_x @Carbon Nanotubes Film with Nest-Like Structure as High-Performance Anode for Lithium-Ion Batteries

Jiaqi Li,^[a] Yang Yang,^[a] Jing Wang,^[a] Peng Zhang,^{*,[b]} and Jinbao Zhao^{*,[a]}

A binder-free nest-like structured MnO_x @carbon nanotubes anode for lithium-ion batteries (LIBs) was prepared through a facile electrophoretic deposition (EPD) method. Through the EPD process, both MnO_2 nanowires and carbon nanotubes (CNTs), as starting materials, were interwoven tightly to form a uniform co-deposited film, possessing a nest-like architecture. After annealing the film under an inert atmosphere, the MnO_2 nanowires transformed into Mn_3O_4 and MnO , as confirmed by

the X-ray diffraction patterns. The nest-like electrode formed a porous and integrated conductive framework and provided the buffer space for the volume change of manganese oxides during cycling processes. As a result, this MnO_x @CNTs electrode exhibited excellent cycling performance with a reversible capacity of $1152.1 \text{ mAh g}^{-1}$ at 0.2 A g^{-1} and a superior cycling stability with 88.0% capacity retention at 1 A g^{-1} after 200 cycles.

1. Introduction

Because of the excessive exploitation of fossil fuels, energy crisis is threatening the human existence.^[1] Alternative energy conversion and storage systems have been extensively studied. After originally commercialized by the SONY Company, high-capacity rechargeable lithium-ion batteries (LIBs) are regarded as one of the most promising sustainable chemical power sources to replace fossil fuels power devices.^[2] As the most common commercial anode in LIBs, graphite shows the limited theoretical capacity of only 372 mAh g^{-1} , far away from the demand for large-scale utilization.^[3] By contrast, transition metal oxides (Fe_xO_y , Mn_xO_y , Co_xO_y , Zn_xO_y , Ni_xO_y , etc.) can react with lithium in a different way: conversion reaction ($\text{M}_x\text{O}_y + 2y \text{ Li}^+ + 2y \text{ e}^- \leftrightarrow y \text{ Li}_2\text{O} + x \text{ M}$, $\text{M} = \text{transition metal}$).^[4] All oxidation states of transition metal oxides can be used to store Li ion, exhibiting high theoretical capacities ($> 600 \text{ mAh g}^{-1}$).^[2,5] Among the wide variety of transition metal oxides, manganese oxides (MnO , Mn_2O_3 , MnO_2 and Mn_3O_4) have received much attention due to their low operation potential, high abundance, low toxicity and environmental friendliness.^[6] Nevertheless, the extensive application of manganese oxides as anode in LIBs is still a big challenge because of their rapid capacity decay arising from the intrinsically low electrical conductivity ($\sim 10^{-8}$ to

$10^{-7} \text{ S cm}^{-1}$)^[7] and structural deformation resulting from huge volume change during the cycling processes.^[8]

Two approaches are proposed to address the concerns. One method is to synthesize nanostructured manganese oxides with special morphology, such as hollow/porous nanospheres,^[5-6] nanowires,^[9] nanobelts,^[10] sponge-like structure,^[11] etc. These novel particles with nanostructure can shorten the diffusion paths of lithium ions and provide the buffer space to accommodate the volume changes during the cycling processes. In addition, the bigger specific surface area of nanoparticles could allow the electrolyte to contact with the electrode materials sufficiently, which could facilitate the lithium-ion transportation. The other method is to introduce carbonaceous materials as a buffer matrix, which can not only improve the electrical conductivity of electrode materials but also construct a stable skeleton to avoid the collapse of the electrode structure.^[6b,12] A lot of efforts have been made to embed the manganese oxides with special morphology into the carbonaceous materials in order to combine the advantages of two approaches mentioned above.^[13] However, as far as we know, the conventional coating method is still used to fabricate these composite materials as the LIBs anode, which has a significant disadvantage.

In the conventional process, a mixing slurry involving active materials, conductive additive (acetylene black), polyvinylidene fluoride (PVDF) binder and N-methyl-2-pyrrolidone (NMP) solvent is coated onto the current collector (copper foil). The use of the polymer binder can cause extra weight of inactive materials, leading to reduction of specific capacity. Besides, polymer binder will hinder the transportation of both lithium ions and electrons. In the previous reports,^[14] we have successfully fabricate binder-free Si-based anodes through an electrophoretic deposition (EPD) method. This economical and versatile coating technique has many advantages including good uniformity, controllable coating thickness, short preparation time and simplicity of large-scale fabrication.^[15] Based on

[a] J. Li, Y. Yang, J. Wang, Prof. J. Zhao
State Key Lab of Physical Chemistry of Solid Surfaces,
Collaborative Innovation Center of Chemistry for Energy Materials
College of Chemistry and Chemical Engineering
Xiamen University
Xiamen University, Xiamen 361005 (China)
E-mail: jbzha@xmu.edu.cn

[b] Dr. P. Zhang
School of Energy Research, College of Energy
Xiamen University
Xiamen University, Xiamen 361102 (China)
E-mail: pengzhang@xmu.edu.cn

Supporting information for this article is available on the WWW under <http://dx.doi.org/10.1002/celc.201600706>

the previous works, we modify this method to prepare LIBs electrode composed of manganese oxides nanowires and carbon nanotubes (CNTs).

In this paper, a nest-like anode structure is synthesized via the EPD route starting from MnO_2 nanowires and CNTs. The zeta potentials of MnO_2 nanowires and CNTs dispersing in the acetone are positively enhanced due to the addition of I_2 . During the deposition process, these two one-dimensional elements interlace mutually to build a nest-like electrode on copper foil. After a heat treatment, MnO_2 nanowires will transform into MnO_x nanowires consisted of MnO and Mn_3O_4 . This porous bionic architecture composed of one-dimensional materials can provide the buffer space to accommodate the volume changes of MnO_x and can be maintained in good condition during the cycling processes as anode in LIBs. Furthermore, the electrical conductivity of the electrode is also enhanced owing to the introduction of CNTs. Therefore, this MnO_x @CNTs electrode, as the anode for LIBs, is able to exhibit superior specific capacity, rate performance and structural stability.

2. Results and Discussion

The principle of EPD fabrication is illustrated in Figure 1. When an electric field is applied between the two electrodes, the

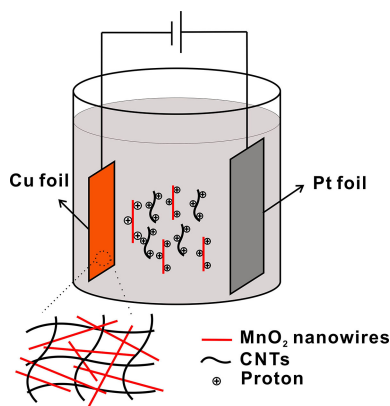


Figure 1. Schematic of the EPD process.

charged particles will move in a definite direction. The MnO_2 nanowires and CNTs are dispersed into the acetone to form EPD suspension. However, these two particles have relatively small ζ potentials (Table 1) and subside rapidly, which is unfavorable for the EPD process. After adding I_2 into the suspension, the I_2 reacts with acetone to release protons.^[16] The generated protons are adsorbed onto the surfaces of particles, making them acquire higher positive ζ potential. As shown in Table 1, the ζ potentials of MnO_2 nanowires and CNTs are dramatically promoted after the addition of I_2 . The positive charges adhering on the particles will repel with each other to form a stable colloid suspension, which is critical for uniform

Table 1. Zeta potential of MnO_2 nanowires and CNTs suspended in acetone and an acetone + I_2 bath.

Concentration in suspension [$\text{g}\cdot\text{L}^{-1}$]				
Sample	MnO_2 nanowires	CNTs	I_2	ζ potential [mV]
1	1	0	0	32.51
2	1	0	1	66.30
3	0	0.4	0	46.80
4	0	0.4	1	61.92
5	1	0.4	1	64.61

deposition. Meanwhile, the enhanced ζ potential will accelerate the mobility of particles under applied electric field.

Figure 2a presents the XRD pattern of as-prepared MnO_2 nanowires which reveals that the precursor can be indexed to

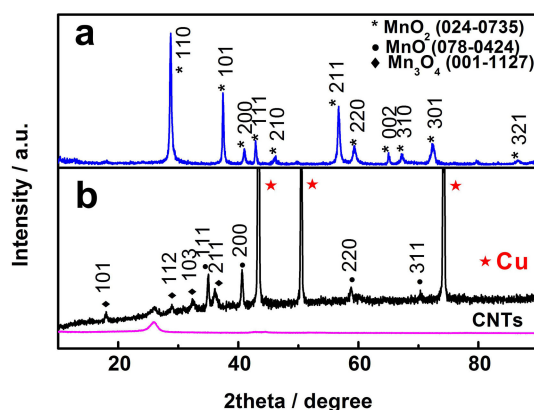


Figure 2. XRD patterns: a) as-prepared $\beta\text{-MnO}_2$ nanowires and b) the MnO_x @CNTs film deposited by using the EPD method.

$\beta\text{-MnO}_2$ (024-0735). The XRD pattern of the post-annealing MnO_x @CNTs electrode is given in Figure 2b. The diffraction signals of Cu foil (070-3038) are so strong that the other peaks are relatively weak. As can be seen, the $\beta\text{-MnO}_2$ precursor transforms into MnO (078-0424) and Mn_3O_4 (001-1127) after the heat treatment, owing to the reduction reaction with mixed carbon nanotubes. The small peak at 26° is consistent with the XRD pattern of the used CNTs. Therefore, this MnO_x @CNTs electrode consists of two kinds of valence manganese oxides (MnO and Mn_3O_4) and carbon nanotubes. Besides, the XRD pattern of the MnO_x @CNTs materials scraped from the Cu foil are also displayed in Figure S2.

Figure 3 shows the SEM images of as-prepared $\beta\text{-MnO}_2$, CNTs and EPD-fabricated MnO_x @CNTs electrode. As illustrated in Figure 3a, the $\beta\text{-MnO}_2$ possesses nanowire morphology with diameters of ≤ 120 nm and lengths of ≤ 5 μm . The SEM image of CNTs is also displayed in the Figure 3b. These two linear materials along with the conductive additive are dispersed into the acetone and adhered onto the Cu foil via electrophoretic deposition. After annealing under argon atmosphere, the MnO_x @CNTs electrode film is obtained, which is only composed of MnO_x nanowires and CNTs without binder. The microstructure of as-prepared electrode is presented in Figure 3c. It can be clearly seen that the MnO_x and CNTs are still maintained

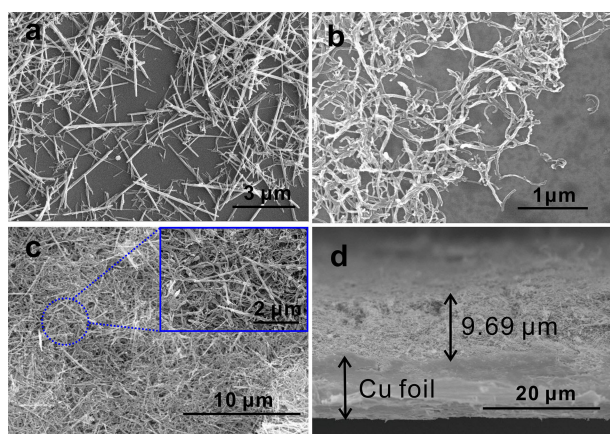


Figure 3. SEM images: a) as-prepared β - MnO_2 nanowires, b) CNTs, c) surface of the EPD-fabricated MnO_x @CNTs film, and d) a cross-section of the EPD-fabricated MnO_x @CNTs film.

one-dimensional morphology after the thermal treatment. Then the two basic elements interlace mutually to build a nest-like architecture, forming a lot of pores on the surface of the electrode. This kind of bionic structure can provide buffer space for accommodating the MnO_x volume changes and avoid the collapse of the electrode structure during the cycling process. Meanwhile, the CNTs interlacing tightly with the MnO_x nanowires could provide an integrated electron conductive network. The thickness of the deposited film is 9.7 μm , as seen from the cross-section (Figure 3d) of the electrode film. And the electrode materials are tightly attached to the Cu foil, without noticeable cracks. The EDS mapping images (Figure 4) demon-

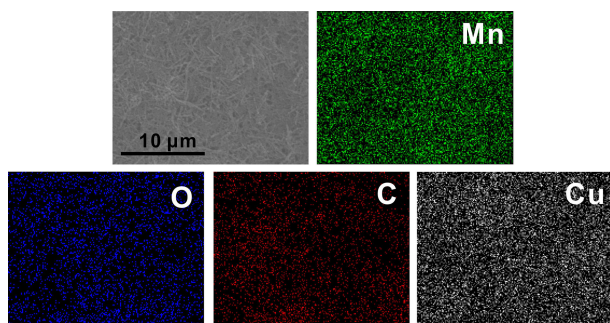


Figure 4. EDS mapping images of co-deposited MnO_x @CNTs electrode.

strate that the MnO_x nanowires and CNTs are evenly co-deposited onto the Cu substrate.

The electrode materials are also investigated by TEM after subjected to ultrasonic exfoliation (shown in Figure 5). It is obviously to distinguish the MnO_x nanowires and CNTs from Figure 5a. The HRTEM image of MnO_x nanowires (Figure 5c) shows the crystalline lattice fringes with two different interlayer spacing. The spacing of 0.31 nm is attributed to the (112) planes of Mn_3O_4 and the spacing of 0.26 nm is consistent with (111) planes of MnO , suggesting the MnO_x is composed of two

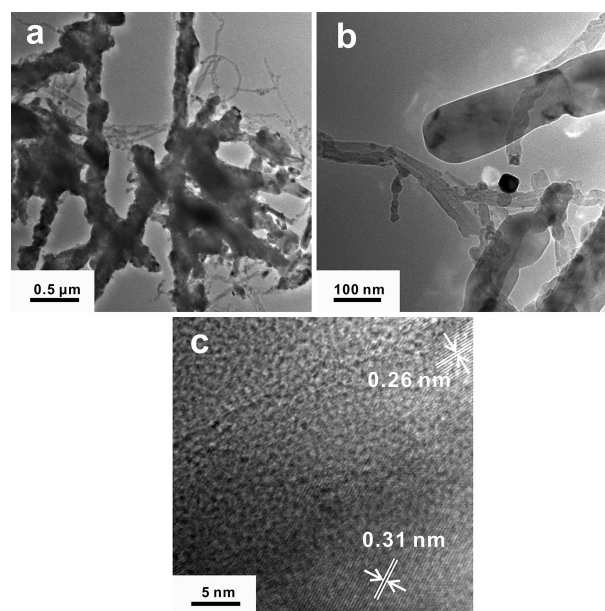


Figure 5. TEM images: a) MnO_x nanowires and b) CNTs. c) HRTEM image of MnO_x .

different phases. This is corresponding to the XRD pattern of the MnO_x @CNTs electrode.

XPS profiles of the MnO_x @CNTs electrode are showed in Figure 6 for the purpose of determining different oxidation states of the MnO_x . The MnO_x @CNTs electrode is composed of C, O and Mn elements, as presented in the survey peaks (Figure 6a) with characteristic C (1 s), O (1 s), Cu (2p) and Mn (2 s, 2p, 3 s and 3p). The peak of Cu (2p) originates from the Cu foil. The high-resolution XPS spectrum of Mn 2p with Mn 2p_{1/2} (653.12 eV) and Mn 2p_{3/2} is given in Figure 6b. The Mn 2p_{3/2} peak are deconvoluted into two peaks with the binding energies of 642.55 eV and 641.20 eV, which are attributed to Mn^{4+} and Mn^{2+} , respectively. The area ratio, which is equivalently to the molar ratio, of Mn^{2+} versus Mn^{4+} is 3.12:1. Therefore, it can be concluded that there is extra MnO except for Mn_3O_4 ($\text{Mn}_3\text{O}_4 = 1 \text{ MnO}_2 + 2 \text{ MnO}$, considering from the stoichiometric ratio), which means the MnO_x is composed of MnO and Mn_3O_4 .^[17]

The content of CNTs are measured by the following process: the electrode materials are peeled off from the co-deposited electrode by ultrasonic treatment in the deionized water. Then the electrode materials are obtained by centrifugation and freeze drying. Subsequently, the CNTs content in electrode materials measured by the elemental analysis instrument is 20.69%.

Figure 7 shows the electrochemical performance of MnO_x @CNTs electrode. Figure 7a represents the CV curves of the MnO_x @CNTs electrode performed from 3.0 to 0.01 V at the scan rate of 0.1 mV s^{-1} . As a comparative figure, the selected discharge/charge profiles of the MnO_x @CNTs electrode at the current density of 0.2 A g^{-1} between 0.01 V and 3 V are also displayed in Figure 7b. In the first cathodic cycle, three reduction peaks are observed from the CV curves. Two small

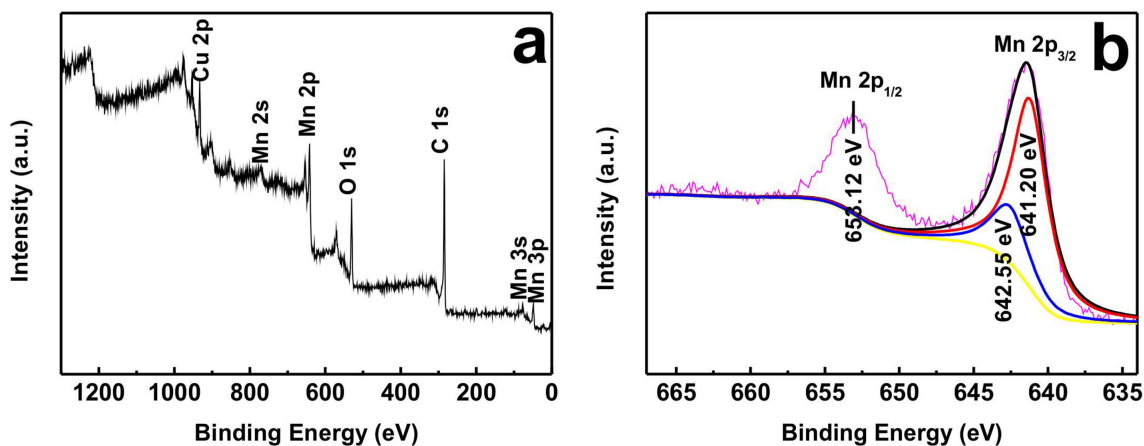


Figure 6. XPS spectra of MnO_x @CNTs electrode: (a) survey scan, (b) high resolution of Mn 2p peaks.

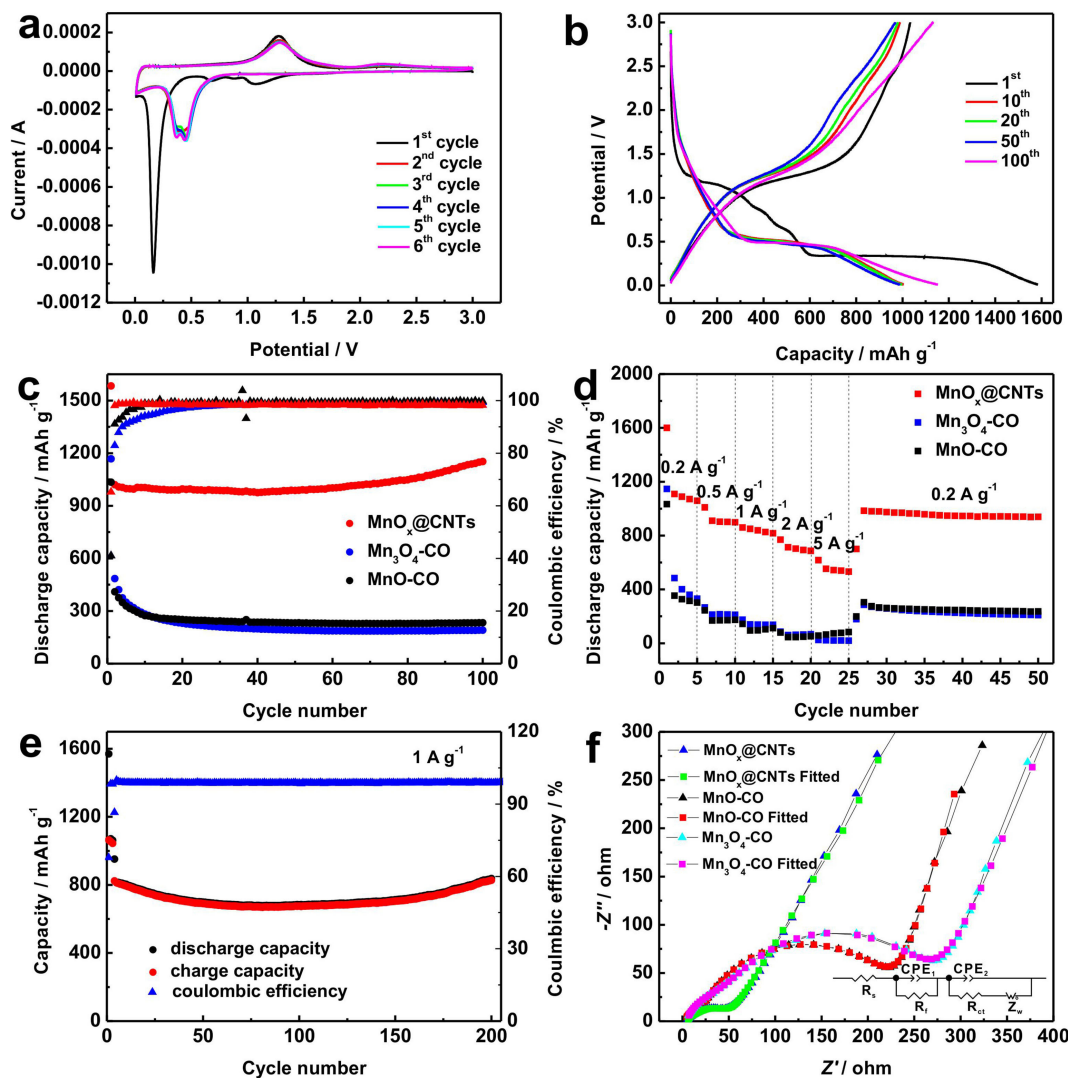


Figure 7. a) CV curves of the EPD-fabricated MnO_x @CNTs electrode at a scan rate of 0.1 mV s^{-1} . b) Selected discharge/charge profiles of the EPD-fabricated MnO_x @CNTs electrode at a current density of 0.2 A g^{-1} . c) Cycle performances of the EPD-fabricated MnO_x @CNTs electrode as well as Mn_3O_4 and MnO electrodes prepared with conventional methods. d) Rate performances of three electrodes at various current densities. e) High rate performance of the EPD-fabricated MnO_x @CNTs electrode at 1 A g^{-1} . f) Nyquist plots of EPD-fabricated MnO_x @CNTs as well as Mn_3O_4 and MnO electrodes fabricated with conventional methods after 10 cycles.

peaks at 0.67 V and 1.07 V observed in the first cathodic CV curves and disappearing afterwards can be ascribed to the decomposition of the electrolyte solvent and the formation of the solid electrolyte interphase (SEI) layer, as well as initial reduction of Mn_3O_4 .^[12c] These two peaks are consistent with the two sloping ranges in the initial discharge cycle shown in Figure 7b. The first sloping range in the initial discharge cycle of Figure 7b between 0.9 V and 1.2 V is consistent with the small peak at 1.07 V in the CV curves while the second short sloping range between 0.45 V and 0.69 V is corresponding well to the small peak at 0.67 V in the CV curves. The intensive and sharp cathodic peak at 0.163 V in the CV curves, which is consistent with the well-defined voltage plateau observed at 0.35 V in the first discharge cycle of Figure 7b, agrees with the conversion of Mn^{2+} to metallic Mn accompanied by the formation of Li_2O . This obvious cathodic peak shifts to 0.37 V in the subsequent cycles because of electrode polarization. In the anodic process, the strong oxidation peak at around 1.28 V and the broad shoulder peak at around 2.20 V appearing in the CV curves are corresponding to the long quasi-plateau at around 1.20 V and the succeeding voltage sloping above 2.35 V during the first charging process in the discharge/charge profiles, respectively. The oxidation of Mn^0 to Mn^{2+} coupled with the decomposition of Li_2O can be account for the strong anodic peak at 1.28 V. While the shoulder peak corresponds to further oxidation of MnO .^[12c] The CV curves become overlapped well with each other after the second cycle, indicating the good reversible electrochemical reactions of the MnO_x @CNTs electrode in the subsequent cycles.

Figure 7c compares the cycling performances of MnO_x @CNTs, Mn_3O_4 -CO and MnO-CO electrodes at 0.2 Ag^{-1} . At the first cycle, MnO_x @CNTs, Mn_3O_4 -CO and MnO-CO electrodes exhibit discharge capacities of 1583.8, 1167.7 and 1034.6 mAhg^{-1} , respectively. The initial coulombic efficiency of MnO_x @CNTs electrode is 65.23%, while that of Mn_3O_4 -CO and MnO-CO electrodes can only reach 41.07% and 41.03%, respectively. After the first cycle, the coulombic efficiency of MnO_x @CNTs electrode rises directly to 98% while it does not increase to 98% until the 30th cycle for Mn_3O_4 -CO electrode and the 10th cycle for MnO-CO electrode. Therefore, the as-prepared MnO_x @CNTs electrode has better electrical conductivity than the comparative samples synthesized via the conventional slurry coating method. In the subsequent cycles, the capacities of Mn_3O_4 -CO and MnO-CO electrodes fade dramatically and finally sustain at 190 and 230 mAhg^{-1} , respectively. However, MnO_x @CNTs electrode maintains a steady high capacity at the initial 40 cycles. After 40 cycles, the capacity of MnO_x @CNTs electrode shows a rising tendency which is normally observed for manganese oxides anode.^[18] Reversible capacity as high as 1152.1 mAhg^{-1} after 100 cycles is achieved, with the discharge capacity retention of 72.7%. The cycle performance of EPD-fabricated MnO_2 @CNTs film without annealing process is also investigated at the current density of 0.2 Ag^{-1} (Figure S1). The coulombic efficiency of MnO_2 @CNTs electrode in the first cycle is only 32.46% although the discharge capacity could reach the relatively high value of

$1673.65 \text{ mAhg}^{-1}$. The discharge capacity decays fast in the subsequent cycles.

The rate performances of MnO_x @CNTs, Mn_3O_4 -CO and MnO-CO electrodes at series of current densities between 0.01 and 3 V are displayed in Figure 7d. The MnO_x @CNTs electrode shows excellent performance. The discharge capacity in the first cycle at 0.2 Ag^{-1} of as-prepared electrode is 1600.9 mAhg^{-1} . Then the average discharge capacities are 924.9, 838.5, 713.2 and 557.6 mAhg^{-1} at gradually raising current densities of 0.5, 1, 2 and 5 Ag^{-1} , respectively. Even more, the high discharge capacity of 984.8 mAhg^{-1} is recovered when the current density comes back again to 0.2 Ag^{-1} , exhibiting an excellent cyclic stability of nest-like MnO_x @CNTs electrode. As for MnO-CO and Mn_3O_4 -CO electrodes, the discharge capacities of various current densities are very low and fade quickly with the increase of current density.

The high-rate cycling performance of MnO_x @CNTs electrode at 1 Ag^{-1} is also given in Figure 7e. For the first 3 cycles the electrode is activated by discharging and charging at the low rate of 0.2 Ag^{-1} and then cycled at 1 Ag^{-1} for the subsequent process. At the beginning of the high rate performance, the discharge capacity is 951.6 mAhg^{-1} . The capacity of 837.4 mAhg^{-1} with the retention of 88.0% can still be obtained after 200 cycles, indicating an excellent performance at high current density.

The excellent electrochemical properties of MnO_x @CNTs electrode are attributed to the following aspects: a) the nest-like architecture offers buffer space for the volume change of MnO_x , which could avoid the collapse of the electrode structure and keep the structure stable during the cycling; b) the introduction of CNTs provides a large-scale conductive network, facilitating the electron transportation among the electrode materials.

In order to explain the superior electrochemical performance of the MnO_x @CNTs electrode, the Nyquist plots of MnO_x @CNTs, MnO-CO and Mn_3O_4 -CO electrodes after 10 cycles are presented in Figure 7f, together with the fitted graphs using the equivalent circuit. All of the curves are composed of two depressed semicircles and one inclined line. Generally, the one semicircle located in the high frequency region indicates the resistance (R_f) and the capacitance (CPE_1) of the SEI layer, while the other semicircle located in the middle frequency region is related to the charge transfer resistance (R_{ct}) through the electrode/electrolyte interface and the double-layer capacitance (CPE_2).^[19] The inclined line located in the low frequency region is corresponding to the diffusion of Li ions in the electrode, known as Warburg impedance (Z_w).^[6c, 20] The fitting data are shown in the Table 2. Obviously, the R_f and the R_{ct} of the MnO_x @CNTs electrode is much smaller than values of the two other electrodes. This result indicates that the interaction of MnO_x and CNTs could reduce the resistance of the SEI layer and promote electron conduction in the electrode. The advantage of MnO_x @CNTs electrode in electron conductivity is ascribed to two reasons: a) the interpenetrating network composed of MnO_x and CNTs makes the contact between two elements more closely and allows the excellent conductivity of CNTs into full play; b) the absence of the binder also alleviates

Table 2. Impedance parameters of MnO_x@CNTs, MnO-CO, and Mn₃O₄-CO electrodes.

Electrode ^[a]	R _f [Ω]	Error [%]	R _{ct} [Ω]	Error [%]
MnO _x @CNTs	2.49	1.59	49.12	3.20
MnO-CO	14.54	4.26	212.10	0.76
Mn ₃ O ₄ -CO	39.44	0.72	237.4	1.54

[a] The MnO_x@CNTs electrode is fabricated by using the EPD method. Both the MnO-CO and Mn₃O₄-CO electrodes are fabricated by using the conventional method.

the loss of electron conductivity owing to the low conductivity of the conventional binder.

3. Conclusions

In summary, a nest-like MnO_x@CNTs electrode has been successfully prepared via EPD process. This unique structure has some major advantages as the anode for LIBs: 1) the nest-like electrode structure can keep stable during the cycling process; 2) the porous channels in different dimensions created by interpenetrating MnO_x nanowires and CNTs enable the electrolyte permeate into the electrode and contact with the active materials more sufficiently; 3) the introduction of highly conductive CNTs can facilitate the electron transportation; 4) the rapid binder-free fabrication of MnO_x@CNTs electrode can also eliminate the influence of the inactive materials. Our results have demonstrated superior electrochemical performances of the EPD-fabricated MnO_x@CNTs.

Experimental Section

Synthesis of MnO₂ Nanowires

MnO₂ nanowires were synthesized by the reported method.^[21] In a typical synthesis, 0.02 mol (NH₄)₂S₂O₈, 0.02 mol MnSO₄·H₂O and 0.0175 mol (NH₄)₂SO₄ were dissolved into 80 mL deionized water. Homogeneous solution was formed after continuously stirring, which was then sealed into a Teflon-lined autoclave. Followed by a heat treatment at 140 °C for 12 h, the black products were obtained. After washing with pure water and ethanol for several times, the final precipitates were dried by freeze-drying for 72 h.

Preparation of MnO_x@CNTs Electrodes

The MnO_x@CNTs electrode was prepared by the EPD method. 0.05 g as-prepared MnO₂, 0.25 g multi-walled carbon nanotubes slurry (wt% = 8%) were added into 50 mL acetone and then the suspension was ultrasonically agitated for 2 h. After that, 0.05 g iodine was added into the suspension. Then the suspension was dispersed by the disperser for 2 h. A platinum film and a copper film immersing in the suspension, separated by the constant distance of 1.5 cm, were designed as the anode and the cathode, respectively. The constant voltage applied between the two electrodes was set to 100 V for 40 s. At the same time the suspension was subjected to magnetic stirring for avoiding the gravitational sedimentation of particles. After dried at 80 °C in a vacuum drying oven for 12 h, the EPD film was thermally treated in

a tube furnace to enhance the cohesion between MnO₂ and CNTs. The treatment temperature was raised to 600 °C with a heating rate of 5 °C min⁻¹ and kept for 4 h under the atmosphere of Ar. Comparative electrodes were prepared through the conventional process. The active materials (commercially used MnO or Mn₃O₄), acetylene black and PVDF binder were mixed in the weight ratio of 70:20:10 with a few drops of NMP to prepare the slurry. Then the slurry was coated onto the Cu foil. After that, the foil was dried at 80 °C under vacuum overnight, forming slurry coated Mn₃O₄ and MnO electrodes (named as Mn₃O₄-CO and MnO-CO electrodes, respectively).

Characterization

The zeta (ζ) potential of particles dispersed into the acetone was measured by NanoBrook 90Plus PALS (Brookhaven Instruments Corporation). X-ray diffraction (XRD) data were scanned at 2° min⁻¹ from 10° to 90° on the Rigaku miniflex 600(40 kV/15 mA) with Cu-Kα radiation. X-ray photoelectron spectroscopy (XPS) experiments were carried out on PHI Quantum 2000 Scanning ESCA Microprobe. The morphological observations and surface distributions of elements on the deposited film were performed by scanning electronic microscopy (SEM) on HITACHI S-4800 equipped with an X-ray spectroscopy accessory (EDS, OXFORD 7593-H). Transmission electron microscopy (TEM) images were obtained by JEOL-2100. The content of CNTs in the co-deposited film was measured by element analysis instrument (Vario EL III, Elementar Analysen System GmbH, Germany).

Electrochemical Measurements

The electrochemical performances were investigated in the coin cells, with measured electrodes and a metal lithium plate as working and counter electrodes, respectively. The cells were assembled under Argon atmosphere in the whole process. The electrolyte was prepared by dissolving 1 M LiPF₆ in 1:1 v/v ethylene carbonate/diethyl carbonate mixture. Galvanostatic discharge/charge cycling tests were operated on a Shenzhen Neware battery cycler within the voltage range of 0.01–3 V (vs Li⁺/Li). Cyclic voltammetry (CV) measurement was conducted on the CHI1030c electrochemical workstation (Shanghai Chenhua) at the scanning rate of 0.1 mV s⁻¹ between 0.01 and 3 V. Electrochemical impedance spectroscopy (EIS) was performed at the frequency range from 0.01 Hz to 100 kHz on the Solartron SI 1287 electrochemical workstation. All of the electrochemical properties were measured at room temperature.

Acknowledgements

The authors gratefully acknowledge financial support from National Natural Science Foundation of China (21273185 and 21321062) and Key Project of Science and Technology of Xiamen (3502Z20141008). The authors also express thanks to Prof. Daiwei Liao of Xiamen University for his valuable suggestions.

Conflict of Interest

The authors declare no conflict of interest.

Keywords: lithium-ion battery · electrophoretic deposition · nest-like structure · manganese oxides nanowires · CNTs

- [1] a) M. T. McDowell, S. W. Lee, W. D. Nix, Y. Cui, *Adv. Mater.* **2013**, *25*, 4966–4985; b) S. Goriparti, E. Miele, F. De Angelis, E. Di Fabrizio, R. Proietti Zaccaria, C. Capiglia, *J. Power Sources* **2014**, *257*, 421–443.
- [2] M. V. Reddy, G. V. Subba Rao, B. V. Chowdari, *Chem. Rev.* **2013**, *113*, 5364–5457.
- [3] M. Winter, J. O. Besenhard, M. E. Spahr, P. Novak, *Adv. Mater.* **1998**, *10*, 725–763.
- [4] a) J. Li, H. Dahn, L. Krause, D.-B. Le, J. Dahn, *J. Electrochem. Soc.* **2008**, *155*, A812–A816; b) Z. Yang, J. Shen, L. A. Archer, *J. Mater. Chem.* **2011**, *21*, 11092–11097; c) C. Chae, J. H. Kim, J. M. Kim, Y.-K. Sun, J. K. Lee, *J. Mater. Chem.* **2012**, *22*, 17870; d) B. Wang, X.-Y. Lu, Y. Tang, W. Ben, *ChemElectroChem* **2016**, *3*, 55–65; e) D. Zhang, Y. Li, M. Yan, Y. Jiang, *ChemElectroChem* **2014**, *1*, 1155–1160.
- [5] X. Jiang, Y. Wang, L. Yang, D. Li, H. Xu, Y. Ding, *J. Power Sources* **2015**, *274*, 862–868.
- [6] a) J. Yue, X. Gu, L. Chen, N. Wang, X. Jiang, H. Xu, J. Yang, Y. Qian, *J. Mater. Chem. A* **2014**, *2*, 17421–17426; b) F. Ma, A. Yuan, J. Xu, *ACS Appl. Mater. Interfaces* **2014**, *6*, 18129–18138; c) Y. Xia, Z. Xiao, X. Dou, H. Huang, X. Lu, R. Yan, Y. Gan, W. Zhu, J. Tu, W. Zhang, *ACS Nano* **2013**, *7*, 7083–7092; d) Z. Cai, L. Xu, M. Yan, C. Han, L. He, K. M. Hercule, C. Niu, Z. Yuan, W. Xu, L. Qu, *Nano Lett.* **2014**, *15*, 738–744.
- [7] Z. Li, N. Liu, X. Wang, C. Wang, Y. Qi, L. Yin, *J. Mater. Chem.* **2012**, *22*, 16640–16648.
- [8] a) Y. Ding, C. Wu, H. Yu, J. Xie, G. Cao, T. Zhu, X. Zhao, Y. Zeng, *Electrochim. Acta* **2011**, *56*, 5844–5848; b) X. Li, D. Li, L. Qiao, X. Wang, X. Sun, P. Wang, D. He, *J. Mater. Chem.* **2012**, *22*, 9189–9194.
- [9] a) H. Pang, Z. Yang, J. Lv, W. Yan, T. Guo, *Energy* **2014**, *69*, 392–398; b) I.-H. Ko, S.-J. Kim, J. Lim, S.-H. Yu, J. Ahn, J.-K. Lee, Y.-E. Sung, *Electrochim. Acta* **2016**, *187*, 340–347; c) Y. Wang, Y. Wang, D. Jia, Z. Peng, Y. Xia, G. Zheng, *Nano Lett.* **2014**, *14*, 1080–1084.
- [10] R. Ma, Y. Bando, L. Zhang, T. Sasaki, *Adv. Mater.* **2004**, *16*, 918–922.
- [11] J. Gao, M. A. Lowe, H. D. Abruna, *Chem. Mater.* **2011**, *23*, 3223–3227.
- [12] a) B. Sun, Z. Chen, H.-S. Kim, H. Ahn, G. Wang, *J. Power Sources* **2011**, *196*, 3346–3349; b) K. Zhang, P. Han, L. Gu, L. Zhang, Z. Liu, Q. Kong, C. Zhang, S. Dong, Z. Zhang, J. Yao, *ACS Appl. Mater. Interfaces* **2012**, *4*, 658–664; c) L. Li, Z. Guo, A. Du, H. Liu, *J. Mater. Chem.* **2012**, *22*, 3600–3605; d) S. Petnikota, V. V. Srikanth, P. Nithyadharseni, M. V. Reddy, S. Adams, B. V. R. Chowdari, *ACS Sustainable Chem. Eng.* **2015**, *3*, 3205–3213.
- [13] a) X. Zhang, T. Wang, C. Jiang, F. Zhang, W. Li, Y. Tang, *Electrochim. Acta* **2016**, *187*, 465–472; b) S. Zhang, W. He, X. Zhang, X. Yang, *J. Mater. Sci. Mater. Electron.* **2015**, *26*, 2189–2197; c) S.-Z. Huang, Y. Cai, J. Jin, J. Liu, Y. Li, Y. Yu, H.-E. Wang, L.-H. Chen, B.-L. Su, *Nano Energy* **2015**, *12*, 833–844; d) C. Zhu, N. Sheng, T. Akiyama, *RSC Adv.* **2015**, *5*, 21066–21073.
- [14] a) Y. Yang, D. Chen, B. Liu, J. Zhao, *ACS Appl. Mater. Interfaces* **2015**, *7*, 7497–7504; b) Y. Yang, J. Li, D. Chen, T. Fu, D. Sun, J. Zhao, *ChemElectroChem* **2016**, *3*, 757–763.
- [15] a) Y. Huang, H. Liu, Y.-C. Lu, Y. Hou, Q. Li, *J. Power Sources* **2015**, *284*, 236–244; b) X. Wu, B. Wang, S. Li, J. Liu, M. Yu, *RSC Adv.* **2015**, *5*, 33438–33444; c) N. P. Benekohal, M. J. Sussman, H.-c. Chiu, M. Uceda, R. Gauvin, G. P. Demopoulos, *J. Electrochem. Soc.* **2015**, *162*, D3013–D3018.
- [16] T. Mathews, N. Rabu, J. R. Sellar, B. C. Muddle, *Solid State Ionics* **2000**, *128*, 0167–2738.
- [17] a) G. An, P. Yu, M. Xiao, Z. Liu, Z. Miao, K. Ding, L. Mao, *Nanotechnology* **2008**, *19*, 275709; b) Y. Sun, X. Hu, W. Luo, F. Xia, Y. Huang, *Adv. Func. Mater.* **2013**, *23*, 2436–2444.
- [18] a) C. Chae, J. H. Kim, J. M. Kim, Y.-K. Sun, J. K. Lee, *J. Mater. Chem.* **2012**, *22*, 17870–17877; b) L. Wang, Y. Li, Z. Han, L. Chen, B. Qian, X. Jiang, J. Pinto, G. Yang, *J. Mater. Chem. A* **2013**, *1*, 8385–8397; c) H. Kim, S.-W. Kim, J. Hong, Y.-U. Park, K. Kang, *J. Mater. Res.* **2011**, *26*, 2665–2671.
- [19] a) G. Zhao, X. Huang, X. Wang, P. Connor, J. Li, S. Zhang, J. T. S. Irvine, *J. Mater. Chem. A* **2015**, *3*, 297–303; b) G. Xu, L. Zhang, C. Guo, L. Gu, X. Wang, P. Han, K. Zhang, C. Zhang, G. Cui, *Electrochim. Acta* **2012**, *85*, 345–351.
- [20] S.-Y. Liu, J. Xie, Y.-X. Zheng, G.-S. Cao, T.-J. Zhu, X.-B. Zhao, *Electrochim. Acta* **2012**, *66*, 271–278.
- [21] X. Wang, Y. Li, *Chem. Eur. J.* **2003**, *9*, 300–306.

Manuscript received: November 8, 2016
Accepted Article published: January 9, 2017
Final Article published: January 27, 2017